materials

MDPI

Article

Effect of Ball Milling on the Absorption Properties of Fe_3O_4

Yi Liang, Yue Yuan, Yuwei Huang, Yujiang Wang *, Shicheng Wei *, Bo Wang *, Wei Huang, Wei Xin and Xinlei Wang

National Key Laboratory for Remanufacturing, Army Academy of Armored Forces, Beijing 100072, China; liangyi365@126.com (Y.L.); yyyue11111@163.com (Y.Y.); hywhuj1607@126.com (Y.H.); HW949963@163.com (W.H.); xw1390332928@126.com (W.X.); wxl111210026@163.com (X.W.)

* Correspondence: hitwyj@126.com (Y.W.); wsc33333@163.com (S.W.); wangbobo421@163.com (B.W.); Tel.: +86-010-66718541 (Y.W.); +86-010-66719084 (S.W.); +86-010-66718540 (B.W.)

Received: 15 January 2020; Accepted: 14 February 2020; Published: 17 February 2020

Abstract: $FeCl_3 \cdot 6H_2O$ was used as raw material to produce Fe_3O_4, using the solvothermal method with ethylene glycol as the solvent. Fe_3O_4, with different particle sizes, was obtained via mechanical ball-milling by controlling the milling time. Effect of the milling time on the structure, morphology, and electromagnetic parameters of Fe_3O_4 were studied, and the absorption properties and mechanism of Fe_3O_4, for different milling times were analyzed. The results showed that the integrity of the original small spherical structure decreased as the ball milling time increased. Fe_3O_4 showed excellent microwave absorptions as the milling time reached 2 h, the reflection loss reached the maximum of −21.19 dB at 4.64 GHz as the thickness was 6.55 mm.

Keywords: ball milling time; microstructure; morphology; electromagnetic parameters

1. Introduction

Thanks to progress in science and technology, electromagnetic waves are now widely used in people's lives. However, there are more only benefits but also problems like pollution. To reduce the impact of electromagnetic waves on the environment, research and development of absorption materials has become a popular research topic [1–5].

As one of the ferrites with an anti-spinel structure, Fe_3O_4 is a common magnetic material, which has the characteristics of low cost, simple production, and good magnetic properties [6–8]. Since it can generate large magnetic losses in alternating electromagnetic fields, Fe_3O_4 is one of the most widely used conventional absorption materials. However, due to the Snoek limitation in the high-frequency region, easy oxidation, high density, and narrow absorption frequency, the comprehensive electromagnetic wave attenuation properties of Fe_3O_4 are also limited. An effective way to improve electromagnetic wave absorption of Fe_3O_4, is to prepare materials with hollow, nanometer-sized structures [9–12]. Hollow structures can increase the attenuation of electromagnetic waves via multiple reflections of the incident electromagnetic waves within the cavity. Due to the high proportion of atoms on the surface of the particles, nanomaterials are prone to interface polarization, which can cause multiple scattering. Moreover, nanomaterials show quantum size effects, which split the electron energy levels of particles, and the splitting interval corresponds to the energy range of electromagnetic waves, which opens a new absorption channel [13–15].

Mechanical ball milling is the simplest and most used method to prepare micro/nano particles. It refers to the method of placing a material into a ball mill and grinding the material to produce broken particles and fine particles via reciprocal action between material and grinding balls. This method is characterized by a simple process and high yield, which is usually divided into two types: dry milling

and wet milling. Wet milling can easily grind the product to a fine size and produce more uniform nanoscale particles.

At present, chemical synthesis is the most common method to prepare electromagnetic wave absorbers with different micro/nano sizes. However, the preparation method is difficult, the required time is long and the yield is low. In addition, the size of the prepared materials is uncertain. Therefore, it is expected to obtain particles with different particle diameters using the simplest mechanical ball-milling method, which is based on the chemical synthesis method. In this paper, the Fe_3O_4, absorption material was synthesized using the hydrothermal method, and the ball milling method was used to study the changes of phase, morphology, structure, and electromagnetic parameters of Fe_3O_4, at different ball-milling times. The effects of structure and size of Fe_3O_4 absorption material on the electromagnetic-wave attenuation performance were analyzed, and the feasibility of preparing nano-absorption-materials using mechanical ball-milling was discussed.

2. Experimental

2.1. Preparation of Fe_3O_4

(1) Preparation of the Fe_3O_4 absorption material: 45 ml of ethylene glycol was placed in a beaker, then, 4 g of urea and 2 g of polyvinyl pyrrolidine were added, and evenly dispersed ultrasonically. Subsequently, 1–2 g of $FeCl_3{\cdot}6H_2O$ was weighed, using an electronic balance, and added to the above solution. Then, ultrasonic treatment was preformed until the $FeCl_3{\cdot}6H_2O$ was uniformly dispersed in the solution. Next, the solution was placed in a 100 ml high-pressure autoclave containing polytetrafluoroethylene, and the reaction was performed at 200 °C for 12 h. After the reaction, the sample was taken out, washed with anhydrous ethanol and distilled water many times, and dried for 24 h in a vacuum drying oven.

(2) Ball milling treatment of the prepared Fe_3O_4: To prevent the introduction of impurities caused by the abrasion of the grinding balls in the ball-mill tank during dry milling, wet milling was used. Fe_3O_4 samples were placed into the ball-mill tank, following the ratio of grinding ball:material:alcohol = 7:4:3, and ball milling for 0, 0.5, 1, 1.5, and 2 h, respectively. After filtration, they were placed in a vacuum-drying oven and dried for 6 h to obtain ball-milled Fe_3O_4 particles. The morphology, structure, surface elements, and the electromagnetic parameters were analyzed using field emission scanning electron microscope (FESEM, JEOLJSM-6500F, Eindhoven, Holland), transmission electron microscopy (TEM, Tecnai-TF20, Oberkochen, German), X-ray diffraction (XRD, D/MAX-2500PC, Rigaku, Tokyo, Japan), X-ray photoelectron spectroscopy (XPS, Thermo Fisher Scientific, Massachusetts, U.S.A) and vector network analyzer (VNA, N5242A, Agilent, USA)SEM, TEM, XRD, XPS, and VNA, respectively. The electromagnetic parameters of the measured samples were prepared by mixing the products (60%) with molten paraffin wax (40%), and placing them into a toroidal mold (Φ_{in} = 3 mm, Φ_{out} = 7 mm) with a thickness of 2.5–3.0mm.

2.2. Testing and Characterization

A high-power turning-target polycrystalline SmartLab XRD (D/MAX-2500PC, Rigaku, Tokyo, Japan) was used, and the test condition was set as Cu target, with a scanning rate of 2°/min and a scanning range of 5–90°. The surface morphology of the samples was analyzed using FESEM (SU-8010, Hitachi, Tokyo, Japan)HitachiThe microstructure of the samples was analyzed using TEM (JEM 2100, Tokyo, Japan). The electromagnetic parameters of the samples were measured using VNA (N5242A, Agilent, Santa Clara, CA, USA), and the filling amount of the samples in paraffin was 40%.

3. Results and Discussion

3.1. Phase Analysis of Fe_3O_4

In order to analyze the effect of ball-milling time on the structure of Fe_3O_4, a polycrystalline target-turning X-ray diffraction analysis was performed. Figure 1 shows the XRD spectra of Fe_3O_4 at different ball-milling times. It was found that the diffraction peaks were sharp and strong, indicating that the prepared nanoparticles had high crystallinity. When the ball-milling time was 0 h, peaks at 30.2°, 35.6°, 43.2°, 53.6°, 57.1°, and 62.4° in the figure corresponded to the crystal planes of (220), (311), (400), (422), (511), and (440), respectively. According to the crystal plane, corresponding to the diffraction peak position, it can be known that the grain was Fe_3O_4. As the ball-milling time increased, the intensity of the diffraction peaks of Fe_3O_4 decreased, while the impurity peaks in the XRD spectra increased. This indicates that the milling energy increased along with the milling time, and the Fe_3O_4 particles broke up. Therefore, the grain size decreased and the material was further refined. However, it was also more prone to undergo oxidation. In this case, the product was a mixture of Fe_3O_4 and Fe_2O_3, and the extension of ball-grinding time affected the crystal structure of Fe_3O_4.

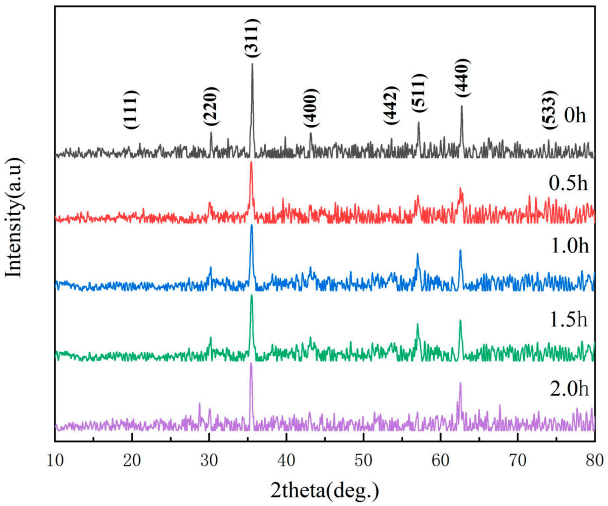

Figure 1. XRD spectra of Fe_3O_4 samples at different milling times.

3.2. Effect of Ball-Milling Time on the Morphology of Fe_3O_4

Figure 2 shows the microstructure of Fe_3O_4 after different ball-milling times. It can be seen from Figure 2a, the Fe_3O_4, prepared using the hydrothermal method, shows a complete and regular spherical shape, with a spherical diameter 300–400 nm. With the increase in milling time, it was found, from Figure 2b–e, that the morphology of the Fe_3O_4 particles changed significantly. The original complete Fe_3O_4 pellets were constantly destroyed, and the particle size significantly reduced. After grinding for 1 h, the dispersion of Fe_3O_4 became worse, and agglomeration was observed. When the ball-milling time reached 2 h, it was observed that most of the Fe_3O_4 was ground into broken particles, and only a few intact pellets remained. The size of the broken Fe_3O_4 particles was 40–80 nm.

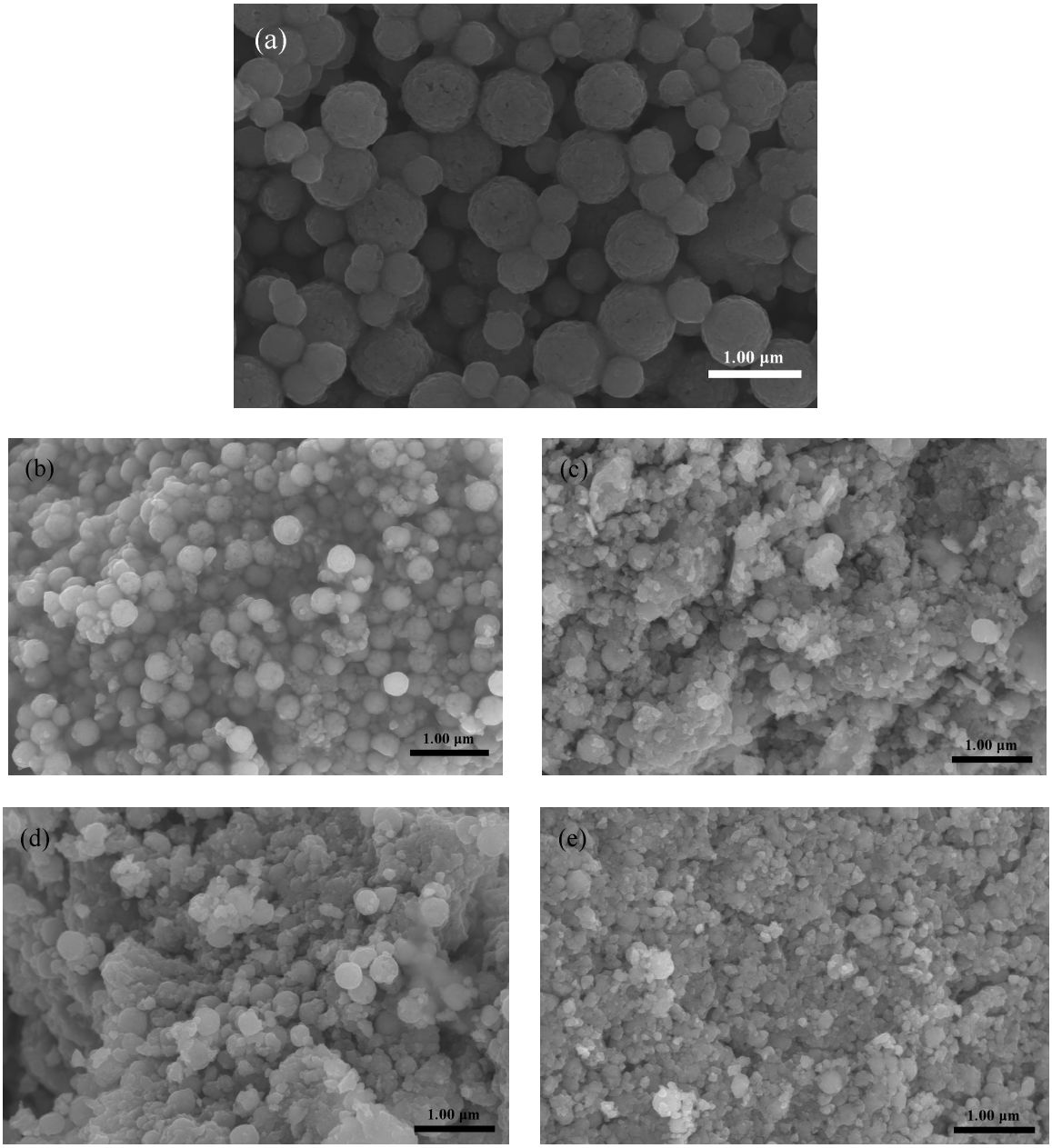

Figure 2. SEM images of Fe_3O_4 samples at different ball-milling times. (**a**) Ball milling for 0 h; (**b**) Ball milling for 0.5 h; (**c**) Ball milling for 1.0 h; (**d**) Ball milling for 1.5 h; (**e**) Ball milling for 2.0 h.

Figure 3 are the TEM images of Fe_3O_4 samples at different ball-milling times. From Figure 3a, it was found that the Fe_3O_4, prepared using the hydrothermal method, showed a complete spherical shape, with a deep edge contrast and shallow center contrast, and the Fe_3O_4 pellets showed a clearly hollow shape. As can be seen from Figure 3b–d, as the ball-milling time increased, the small Fe_3O_4 pellets were continuously broken, the integrity of the spherical particles continued to decline, and the particles became gradually fragmentated. Local agglomeration also occurred, while the size of the broken particles decreased. In general, the hollow structure of the Fe_3O_4 absorption material was continuously destroyed with grinding time, but the particle size of the material was continuously reduced. This is consistent with the results observed using SEM.

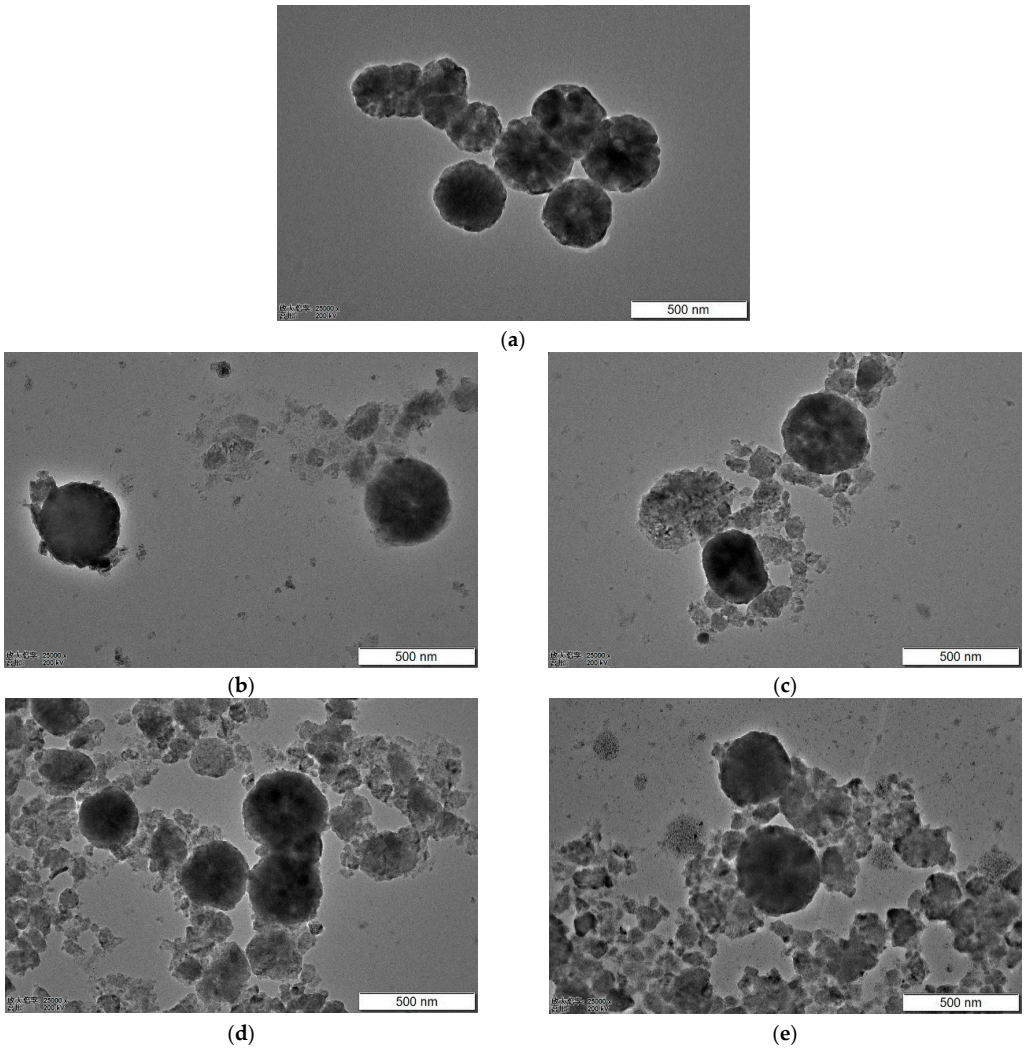

Figure 3. TEM images of Fe_3O_4 at different ball-milling times. (**a**) Ball milling for 0 h; (**b**) Ball milling for 0.5 h; (**c**) Ball milling for 1 h; (**d**) Ball milling for 1.5 h; (**e**) Ball milling for 2.0 h.

3.3. Electromagnetic Parameter Analysis of Fe_3O_4 at Different Ball-Milling Times

Figure 4 shows the curves of the complex permittivity and complex permeability of the Fe_3O_4 absorption material for different grinding times, changing with frequency. Figure 4a shows the curve of the real part of the complex permittivity of the absorption material as a function of frequency. As can be seen from the figure, the real part of the complex permittivity decreased before it increased with increasing ball-grinding time. When the ball-milling time was 1.5 h, the real part was the smallest, and when the milling time reached 2 h, the real part started to increase. Figure 4b displays the curve of the imaginary part of the complex permittivity of the Fe_3O_4 absorption material, as a function of frequency. It was found that the imaginary part of the complex permittivity decreased first with increasing ball-milling time and then remained basically unchanged. The value that varied with frequency was basically the same. Moreover, wave peaks appeared around 4 GHz, 9 GHz, and 15 GHz, indicating that the products had a strong dielectric loss capability at these three frequencies. The imaginary part of the complex permittivity of the Fe_3O_4 absorption material decreased as the ball milling time increased. This is because the originally spherical Fe_3O_4 particles were destroyed after ball milling. For the same mass of powder, the hollow Fe_3O_4 pellets (with low density) added more materials than the high dense Fe_3O_4 fragments, and its distribution in paraffin is also greater. Due to the increased contact area, a large number of hollow Fe_3O_4 spheres formed a macroscopic conductive chain or local conductive network in the material, under the action of the electromagnetic field. Therefore, in the

absence of ball grinding, the absorption material with a large amount of Fe_3O_4 hollow pellets, had both a higher electrical conductivity and dielectric constant. As the ball-milling time increased, the small spherical structures of Fe_3O_4 were destroyed, which resulted in a decrease in electrical conductivity and permittivity of the material. The Fe_3O_4 pellets were ground when the ball-milling time reached 2 h. However, due to sufficient ball-grinding time, the size of the broken particles was smaller and it was easier to form a conductive network. The conductivity of the material showed a rising trend, and the permittivity increased significantly, especially at high frequencies.

Figure 4c,d shows the curves of the real and imaginary parts of the complex permeability of the Fe_3O_4 absorption material, as a function of frequency. As shown in the figures, with increasing frequency, both real and imaginary parts of the complex magnetic permeability of Fe_3O_4, at different ball-milling times, decreased continuously and remained unchanged afterwards. It gradually decreased with the increase of ball-milling time. This is because, when the hollow balls were ground, the material lost the advantage of the hollow structure and reduced the reflection loss of incident electromagnetic waves in the cavity. This, thus, reduced the magnetic loss capacity of the absorption material. However, the imaginary part of the magnetic permeability changed slightly with the ball-milling time, which indicates that the destruction of the hollow small sphere structure of Fe_3O_4 had no significant effect on the magnetic loss of the material.

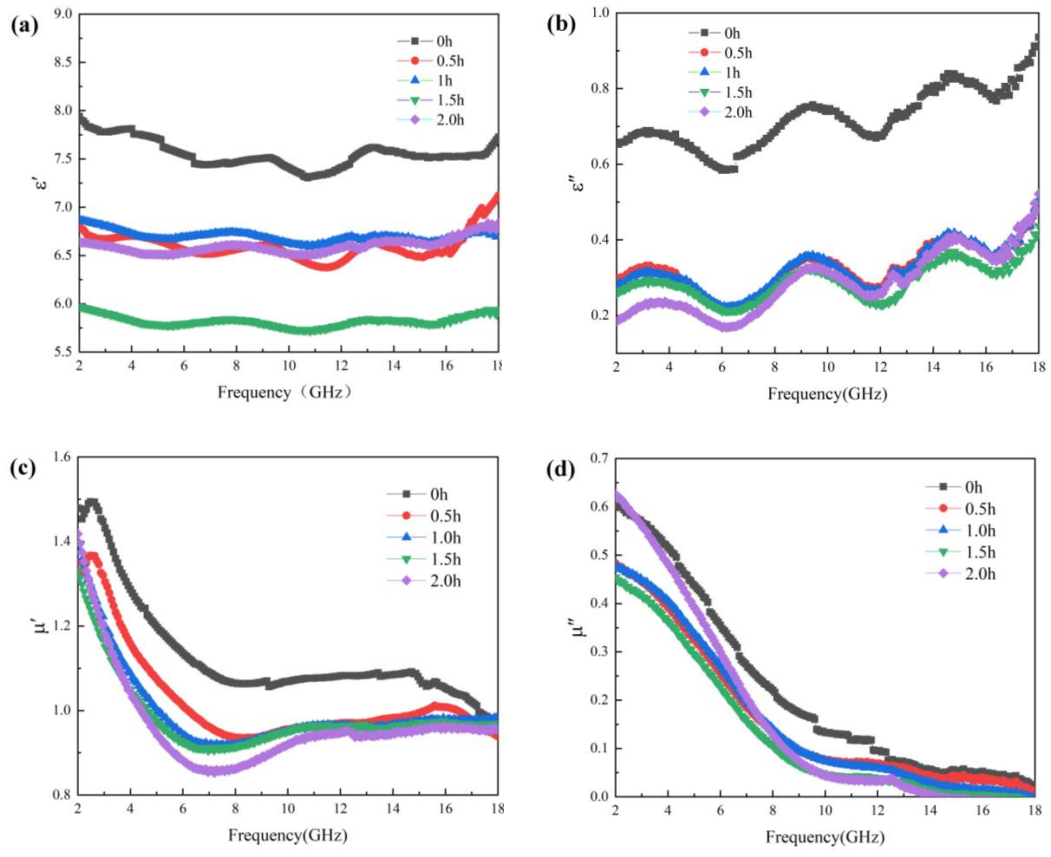

Figure 4. Complex permittivity and complex permeability of the Fe_3O_4 absorption material at different grinding times. (**a**) Real part of the complex permittivity; (**b**) Imaginary part of the complex permittivity; (**c**) Real part of the complex permeability; (**d**) Imaginary part of the complex permeability.

The electromagnetic wave loss factor is usually used to characterize the absorption attenuation capacity of a material, and it can be described as [16]

$$\tan \delta = \tan \delta_E + \tan \delta_M \quad (1)$$

In the formula: $\tan\delta_E$ is the tangent of electrical loss, $\tan\delta_E = \varepsilon''/\varepsilon'$; $\tan\delta_M$ is the tangent of magnetic loss, $\tan\delta_M = \mu''/\mu'$. Among them, ε'' and ε' are the imaginary and real parts of the complex permittivity, and μ'' and μ' are the imaginary and real parts of the complex permeability, respectively. It can be seen that materials with better electromagnetic-wave attenuation can be obtained by increasing the imaginary part and lowering the real part of the absorption material.

Figure 5 shows the dielectric loss tangent and magnetic loss tangent of Fe_3O_4 absorption material at different ball milling times. From Figure 5a,b, it can be seen that, with increasing ball-milling time, the electrical loss tangent of Fe_3O_4 absorption material gradually decreased in the low frequency band. However, in the high frequency band, it first decreased before it increased. This is explained as follows: During the ball milling process, the fragmentation degree of small spherical Fe_3O_4 absorption material improved continuously. This reduced the micro-interface of the absorption material on the whole, weakened the multiple reflection of the incident electromagnetic wave inside the material structure, and further degraded the interface polarization and dielectric loss of the Fe_3O_4 absorption material. On the other hand, as the milling time reached 2 h, even though the small spherical Fe_3O_4 was basically broken, due to the sufficient ball-milling time, the broken particles were ground into finer and more uniform nano-sized particles. Compared with other short-time grinding, the conductivity and dielectric loss of the Fe_3O_4 absorption materials were improved, especially in the high-frequency band.

The effect of different ball-milling times on the magnetic loss tangent of Fe_3O_4 absorption material was not obvious, which indicates that with the extension of the ball-milling time, although the Fe_3O_4 absorption material was gradually broken from the original small spherical shape into fine particles and the structure of the material changed significantly, it had no effect on its magnetic loss. Therefore, changing the microstructure of Fe_3O_4 absorption material via ball milling mainly affected the dielectric properties of the material.

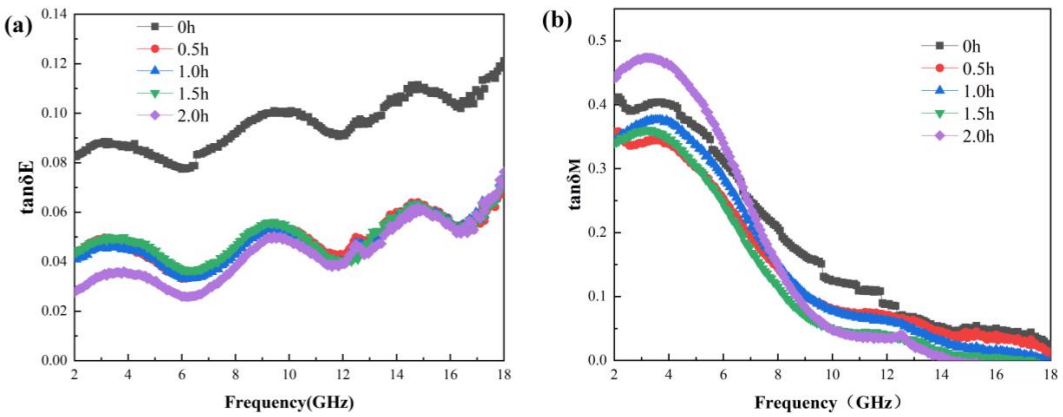

Figure 5. Electric loss tangent and magnetic loss tangent of the Fe_3O_4 absorption material at different grinding times. (**a**) Dielectric loss tangent; (**b**) Magnetic loss tangent.

3.4. Electromagnetic-Wave Attenuation Mechanisms of Fe_3O_4 at Different Ball-Milling Times

3.4.1. Effect of Ball-Milling Time on the Absorption Mechanism

Through the analysis of electromagnetic parameters and loss factor, it was implied that the microstructure of the Fe_3O_4 absorption material was changed by ball milling, and its dielectric loss was greatly affected by the refining material size. To learn more about the dielectric loss, Cole–Cole diagrams were used to study the dielectric properties of Fe_3O_4 absorption material at different ball-milling times.

The formula for the permittivity with different frequencies [17] was proposed by K. S. Cole and R. H. Cole

$$\varepsilon - \varepsilon_\infty = \frac{\varepsilon_S - \varepsilon_\infty}{1 + (j\omega\tau_0)^{1-\alpha}} \quad (2)$$

Here, τ_0, α, ε_∞, and ε_S represent the relaxation time, parameter variable, optical frequency permittivity and static dielectric constant, respectively. The complex permittivity ε can be expressed by as [18]

$$\varepsilon = \varepsilon' - j\varepsilon'' \tag{3}$$

The real part ε' and imaginary part ε'' of the permittivity are

$$\varepsilon' = \varepsilon_\infty + \frac{\varepsilon_S - \varepsilon_\infty}{1 + (\omega\tau)^2} \tag{4}$$

$$\varepsilon'' = \frac{\sigma_r + \sigma_R}{\omega\varepsilon_0} + \frac{(\varepsilon_S - \varepsilon_\infty)\omega\tau}{1 + (\omega\tau)^2} \tag{5}$$

The Cole–Cole circular equation for the real and imaginary parts of the complex permittivity can be obtained by combining Equations (3) and (4).

$$\left(\varepsilon' - \frac{\varepsilon_S + \varepsilon_\infty}{2}\right)^2 + \left(\varepsilon'' - \frac{\sigma_r + \sigma_R}{\omega\tau}\right)^2 = \left(\frac{\varepsilon_S - \varepsilon_\infty}{2}\right)^2 \tag{6}$$

It can be seen that the center coordinates were $(\frac{\varepsilon_S+\varepsilon_\infty}{2}, \frac{\sigma\varepsilon_r+\sigma_R}{\omega\tau})$, and the radius was $\frac{\varepsilon_S-\varepsilon_\infty}{2}$. Thus, Cole–Cole diagrams of the Fe_3O_4 absorption material, at different ball milling times, can be obtained—see Figure 6.

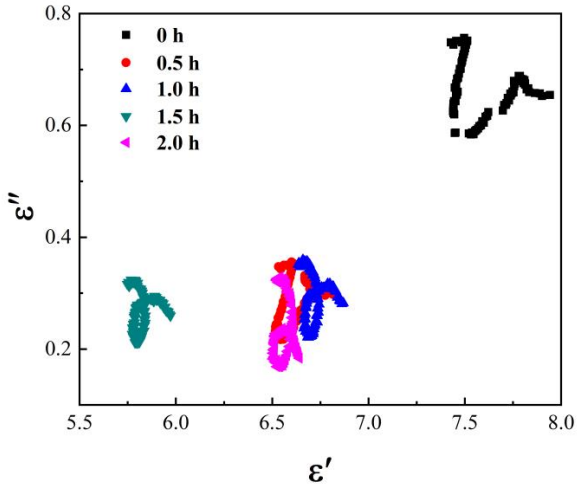

Figure 6. Cole–Cole diagram of the Fe_3O_4 absorption material at different ball-milling times.

According to the center coordinates and radii in Figure 6, the optical frequency permittivity ε_∞, the static permittivity ε_s, and the conductivity σ = σr + σR can be calculated. It can be seen that the semi-circle radius and vertical coordinate of the material, after ball grinding, decreased before it increased. This indicates that the optical frequency permittivity ε_∞ and static permittivity ε_s decreased, after ball milling, and the electric conductivity first decreased and then increased, which is consistent with the results of the dielectric-loss analysis. Therefore, although the dielectric loss of the Fe_3O_4 absorption material can be improved using a sufficiently long ball-milling time, the overall dielectric-loss decreases more than that for the hollow small spherical Fe_3O_4 without ball grinding. Its absorption mechanism was the same as the polarization relaxation before ball milling, and both involve interfacial polarization and dipole polarization relaxation loss.

The loss mechanisms of magnetic loss materials mainly include hysteresis loss, eddy current loss, domain-wall resonance, natural resonance, exchange resonance, and others. In general, hysteresis loss is small in weak external magnetic fields, and domain-wall resonance occurs for the range of 1–100 MHz. Using Aharroni's theory, when one dimension of a nanomaterial is reduced to the nanometer level,

it may generate a resonance mode with higher resonance than the natural resonance. The exchange resonance has been confirmed in many studies. The particle size of the Fe_3O_4 absorption material, prepared via ball milling, was within the nanometer range. Hence, there was some exchange resonance loss. To study the loss of magnetic absorption materials, the following formula is generally used [19]

$$\mu''(\mu')^{-2}f^{-1} = \frac{2}{3}\pi\mu_0 d^2\sigma \quad (7)$$

Here, σ is the conductivity of the material, and μ_0 is the vacuum permeability. In other words, if there is only eddy-current loss, the right side of the formula should be constant. Based on the calculation of electromagnetic parameters, the $\mu''(\mu')^{-2}f^{-1}$ vs. frequency curve of the Fe_3O_4 absorption material at different milling time was obtained—see Figure 7. It can be seen that as the ball-milling time increased, and the $\mu''(\mu')^{-2}f^{-1}$ C0 value of the sample increased for the frequency range of 2–8 GHz. This indicates that the sample's natural resonance-loss capacity at 4–6 GHz increased after ball milling. This was attributed to the enhanced anisotropy of the magnetic crystals after ball milling, which leads to the enhanced anisotropic field, the internal equivalent field enhancement of the ferromagnet, and the increased energy consumption generated by the damping effect. At 8–18 GHz, $\mu''(\mu')^{-2}f^{-1}$ remained basically unchanged, and the eddy-current loss was the main absorption mechanism at this time.

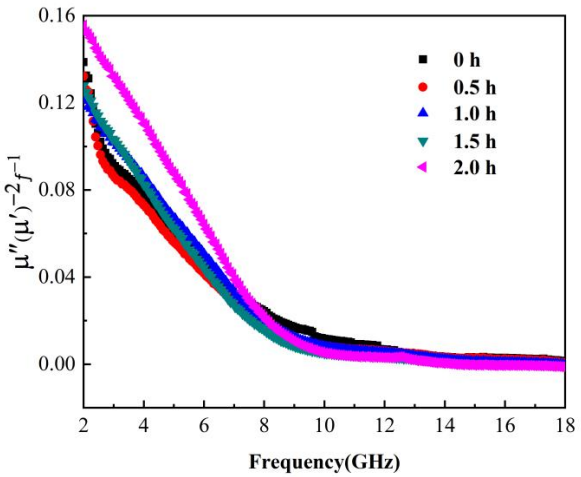

Figure 7. $\mu''(\mu')^{-2}f^{-1}$ vs. frequency curve of the Fe_3O_4 absorption material at different ball-milling times.

3.4.2. Effects of Ball-Milling Time on Absorption

To study the absorption of materials, reflectivity was simulated using MATLAB software, based on the electromagnetic parameters measured by a vector network analyzer. The electromagnetic wave absorption capacity was expressed by the reflection loss RL (dB) as [20]

$$Z_{in} = \sqrt{\frac{\mu_r}{\varepsilon_r}}\tanh\left[j\left(\frac{2\pi fd}{c}\right)\sqrt{\mu_r\varepsilon_r}\right] \quad (8)$$

$$\mathrm{RL(dB)} = 20\log\left|\frac{Z_{in}-1}{Z_{in}+1}\right| \quad (9)$$

Here, h is the Planck constant, c is the speed of electromagnetic waves in vacuum, f is the frequency, d is the thickness of the material, Zin is the input impedance, μ_0 and ε_0 are the permeability and permittivity of free space, ε_r and μ_r are the permittivity and magnetic permeability of the material.

It can be seen from Figure 8 that the small spherical Fe_3O_4, without ball grinding, had a good absorption performance. When the matching thickness was 5.94 mm, it had the largest reflection loss capability at 3.84 GHz, and the reflection-loss reached −20.17 dB. When the matching thickness was

5.24 mm, it had the maximum reflection-loss capability at 15.28 GHz, reaching −41.25 dB. When the matching thickness was 5.98 mm, it showed the maximum reflection loss capability at 13.12 GHz, and the maximum reflection loss was 38.39 dB. This indicates that it had good absorption at both low and high frequencies.

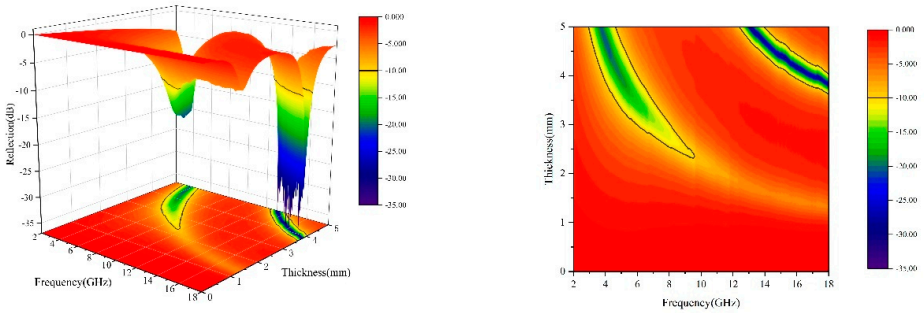

(**a**)

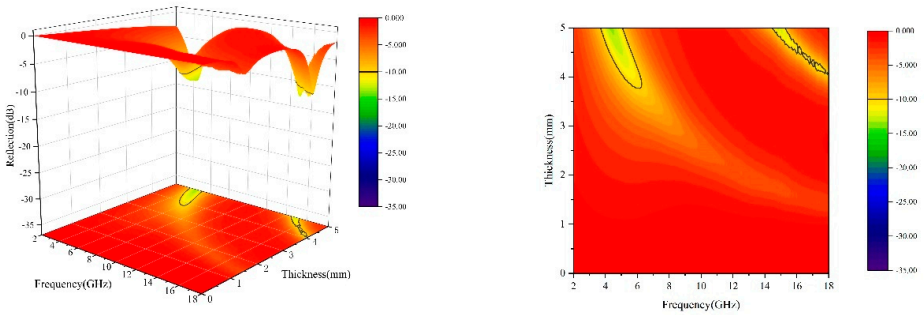

(**b**)

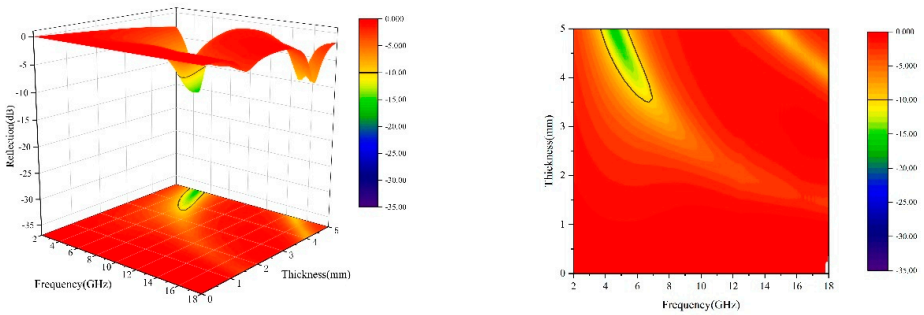

(**c**)

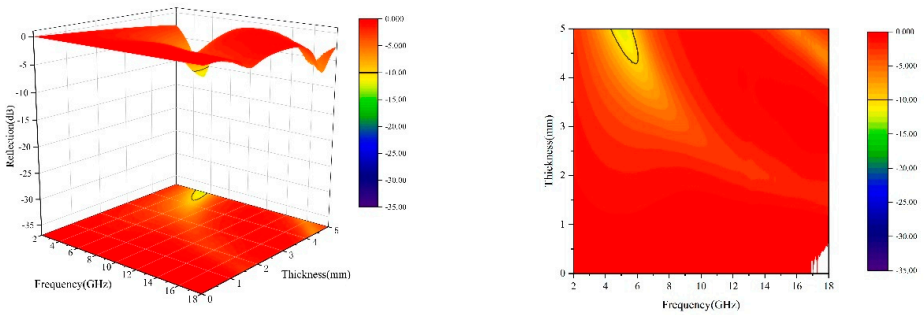

(**d**)

Figure 8. *Cont.*

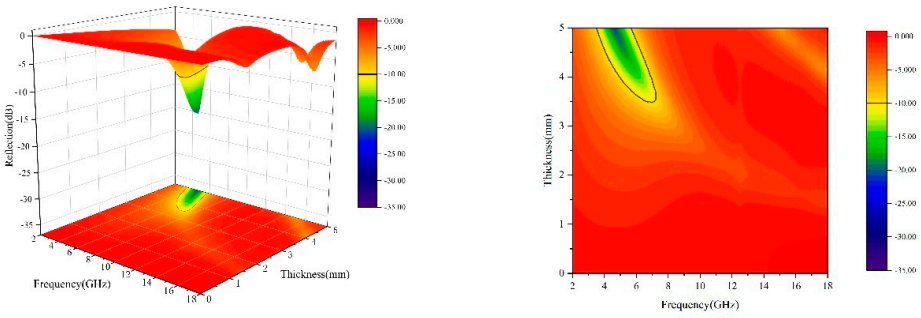

(**e**)

Figure 8. Three-dimensional reflectivity graphs of the Fe_3O_4 absorption materials at different ball milling times. (**a**) Ball milling for 0 h; (**b**) Ball milling for 0.5 h; (**c**) Ball milling for 1 h; (**d**) Ball milling for 1.5 h; (**e**) Ball milling for 2.0 h.

However, as the ball-milling time increased, the absorption of Fe_3O_4 first decreased before it increased. This was because, when the hollow spherical Fe_3O_4 was ball milled, the hollow structure of the surface was destroyed, and the multiple reflection ability was reduced. Although the obtained Fe_3O_4 fragment particles were much finer, the overall electromagnetic wave attenuation performance still showed a significant decline. After ball milling for 0.5 h, the absorption performance of Fe_3O_4 decreased significantly, which suggest that the hollow spherical microstructure had a significant effect on the absorption of Fe_3O_4. With the extension of the ball-milling time, when the ball-milling times were 1 h and 1.5 h, a large number of Fe_3O_4 pellets were broken, the hollow structure severely damaged, and the dielectric loss continued to decrease. Thus, its maximum reflection loss at high frequencies was lower than −10 dB. However, as the ball-milling time continued to increase to 2 h, the spherical structure was almost ball-milled into finer nanoparticles. Because its nanoparticles were smaller in size and had a large specific surface area, it was beneficial to improve the absorption performance of Fe_3O_4. Therefore, compared with other ball grinding times, the absorption of Fe_3O_4 was significantly improved. When the matching thickness was 6.55 mm, there was a large reflection loss at 4.64 GHz, and the maximum reflection loss was −21.19 dB.

4. Conclusions

Effect of ball milling time on microstructure and absorption properties of Fe_3O_4 were investigated systematically. According to the above results, conclusions can be summarized at these following aspects.

1. The integrity and size of Fe_3O_4 particles all decreased as the ball milling time increased. The size of Fe_3O_4 particles decreased from 400 nm to 40 nm.
2. The electromagnetic wave attenuation of hollow spherical Fe_3O_4 reduced by ball milling. More reflective interfaces and better conductive networks of hollow spherical Fe_3O_4 can be formed compared with smaller-sized nanoparticles. When the thickness of non-milled small spherical Fe_3O_4 absorption material was 5.24 mm, the reflection loss reached the maximum value −41.25 dB at 15.28 GHz.
3. Fe_3O_4 showed excellent absorption properties as the milling time reached 2 h. When the thickness was 6.55 mm, the reflection loss reached the maximum of −21.19 dB at 4.64 GHz.

Author Contributions: Y.L., B.W., and Y.W. designed the experiments; Y.Y., Y.H., W.H., W.X. and X.W. performed the experiments; Y.Y. and W.H. analyzed the data; Y.L., Y.Y., and B.W. wrote the paper; S.W. provided theoretical direction; Y.L., B.W., and S.W. provided funding acquisition. All authors have read and agreed to the published version of the manuscript.

Funding: The work was supported by the National Natural Science Foundation of China (Project 51675533, 51701238, and 51905543), Equipment pre-research sharing technology project of "13th Five-Year Plan" (41404010205) and China Postdoctoral Science Foundation Funded Projects (2018M643857).

Conflicts of Interest: The authors declare no conflict of interest.

References

1. Su, X.; Wang, J.; Zhang, X.; Zhang, B.; Wu, Q.; Dai, W.; Zou, Y.; Shao, C. Synthesis of core-shell Fe_3O_4@ppy/graphite nanosheets composites with enhanced microwave absorption performance. *Mater. Lett.* **2019**, *239*, 136–139. [CrossRef]
2. Zong, M.; Huang, Y.; Zhao, Y.; Sun, X.; Qu, C.; Luo, D.; Zheng, J. Facile preparation, high microwave absorption and microwave absorbing mechanism of RGO–Fe_3O_4 composites. *RSC Adv.* **2013**, *3*, 23638. [CrossRef]
3. Fu, C.; He, D.; Wang, Y.; Zhao, X. Facile synthesis of porous Fe_3O_4@C core/shell nanorod/graphene for improving microwave absorption properties. *RSC Adv.* **2018**, *8*, 15358–15365. [CrossRef]
4. Li, Z.W.; Yang, Z.H. Microwave absorption properties and mechanism for hollow Fe_3O_4 nanosphere composites. *J. Magn. Magn. Mater.* **2015**, *387*, 131–138. [CrossRef]
5. Zhang, K.; Zhang, Q.; Gao, X.; Chen, X.; Wang, Y.; Li, W.; Wu, J. Effect of absorbers' composition on the microwave absorbing performance of hollow Fe_3O_4 nanoparticles decorated CNTs/graphene/C composites. *J. Alloys Compd.* **2018**, *748*, 706–716. [CrossRef]
6. Chuangang, H.; Zhongyu, M.; Gewu, L.; Nan, C.; Zelin, D.; Minjia, H.; Liangti, Q. 3D graphene-Fe_3O_4 nanocomposites with high-performance microwave absorption. *Phys. Chem. Chem. Phys.* **2013**, *15*, 13038–13043.
7. Peng, Z.; Jiang, W.; Wang, Y.; Zhong, S. Synthesis and microwave absorption properties of Fe_3O_4@$BaTiO_3$/reduced graphene oxide nanocomposites. *J. Mater. Sci. Mater. Electron.* **2016**, *27*, 1304–1313. [CrossRef]
8. Wang, Z.; Wu, L.; Zhou, J.; Jiang, Z.; Shen, B. Chemoselectivity-induced multiple interfaces in MWCNT/Fe_3O_4@ZnO heterotrimers for whole X-band microwave absorption. *Nanoscale* **2014**, *6*, 12298–123021. [CrossRef] [PubMed]
9. Peng, S.; Sun, S. Synthesis and characterization of monodisperse hollow Fe_3O_4 nanoparticles. *Angew. Chem. Int. Ed.* **2010**, *46*, 4155–4158. [CrossRef] [PubMed]
10. Bin, Q.; Zhu, C.L.; Li, C.Y.; Zhang, X.T.; Chen, Y.J. Coupling hollow Fe_3O_4-Fe nanoparticles with graphene sheets for high-performance electromagnetic wave absorbing material. *ACS Appl. Mater. Interfaces* **2016**, *8*, 3730–3735.
11. Pastore, R.; Delfini, A.; Micheli, D.; Vricella, A.; Marchetti, M.; Santoni, F.; Piergentili, F. Carbon foam electromagnetic mm-wave absorption in reverberation chamber. *Carbon* **2019**, *144*, 63–71. [CrossRef]
12. Qiao, M.; Lei, X.; Ma, Y.; Tian, L.; He, X.; Su, K.; Zhang, Q. Application of yolk–shell Fe_3O_4@N-doped carbon nanochains as highly effective microwave-absorption material. *Nano Res.* **2018**, *11*, 1500–1519. [CrossRef]
13. Wang, A.; Lu, Y.; Sun, R. Recent progress on the fabrication of hollow microspheres. *Mater. Sci. Eng. A* **2007**, *460*, 1–6. [CrossRef]
14. Zhang, S.; Qi, Z.; Yun, Z.; Jiao, Q.; Xiang, N.; Wang, Y.; Yuan, C.; Chang, D. Core/shell structured composites of hollow spherical $CoFe_2O_4$ and CNTs as absorbing materials. *J. Alloys Compd.* **2017**, *694*, 309–312. [CrossRef]
15. Tang, X.T.; Wei, G.T.; Zhu, T.X.; Sheng, L.M.; An, K.; Yu, L.M.; Liu, Y.; Zhao, X.L. Microwave absorption performance enhanced by high-crystalline graphene and $BaFe_{12}O_{19}$ nanocomposites. *J. Appl. Phys.* **2016**, *119*, 204301. [CrossRef]
16. Shi, X.L.; Cao, M.; Yuan, J.; Zhao, Q.; Kang, Y.; Fang, X.; Chen, Y. Nonlinear resonant and high dielectric loss behavior of CdS/α-Fe_2O_3 heterostructure nanocomposites. *Appl. Phys. Lett.* **2008**, *93*, 183118. [CrossRef]
17. Cole, K.S.; Cole, R.H. Dispersion and Absorption in Dielectrics II. Direct Current Characteristics. *J. Chem. Phys.* **2004**, *10*, 98–105. [CrossRef]
18. Liu, X.G.; Jiang, J.J.; Geng, D.Y.; Li, B.Q.; Zhang, Z.D. Dual nonlinear dielectric resonance and strong natural resonance in Ni/ZnO nanocapsules. *Appl. Phys. Lett.* **2009**, *94*, 53119. [CrossRef]
19. Liu, X.; Chen, Y.; Hao, C.; Ye, J.; Yu, R.; Huang, D. Graphene-enhanced microwave absorption properties of Fe_3O_4/SiO_2 nanorods. *Compos. Part. Appl. Sci. Manuf.* **2016**, *89*, 40–46. [CrossRef]
20. Green, M.; Liu, Z.; Xiang, P.; Liu, Y.; Zhou, M.; Tan, X.; Huang, F.; Liu, L.; Chen, X. Doped, conductive SiO_2 nanoparticles for large microwave absorption. *Light Sci. Appl.* **2018**, *7*, 1–9. [CrossRef] [PubMed]